micromachines

MDPI

Article

Ultra Narrow Dual-Band Perfect Absorber Based on a Dielectric—Dielectric—Metal Three-Layer Film Material

Bin Liu [1,2], Pinghui Wu [3], Hongyang Zhu [4,*] and Li Lv [4,*]

1 Rural Revitalization Institute, Linyi University, Linyi 276000, China; liubin@lyu.edu.cn
2 Center for International Education, Philippine Christian University, Manila 1004, Philippines
3 Fujian Provincial Key Laboratory for Advanced Micro-Nano Photonics Technology and Devices, Quanzhou Normal University, Quanzhou 362000, China; phwu@zju.edu.cn
4 School of Physics and Electronic Engineering, Linyi University, Linyi 276000, China
* Correspondence: zhuhongyang@lyu.edu.cn (H.Z.); lvli@lyu.edu.cn (L.L.)

Abstract: This paper proposes a perfect metamaterial absorber based on a dielectric—dielectric—metal structure, which realizes ultra-narrowband dual-band absorption in the near-infrared band. The maximum Q factor is 484. The physical mechanism that causes resonance is hybrid coupling between magnetic polaritons resonance and plasmon resonance. At the same time, the research results show that the intensity of magnetic polaritons resonance is much greater than the intensity of the plasmon resonance. By changing the structural parameters and the incident angle of the light source, it is proven that the absorber is tunable, and the working angle tolerance is 15°. In addition, the sensitivity and figure of merit when used as a refractive index sensor are also analyzed. This design provides a new idea for the design of high-Q optical devices, which can be applied to photon detection, spectral sensing, and other high-Q multispectral fields.

Keywords: dielectric; narrowband; metamaterial perfect absorber; high-Q; tunability

Citation: Liu, B.; Wu, P.; Zhu, H.; Lv, L. Ultra Narrow Dual-Band Perfect Absorber Based on a Dielectric—Dielectric—Metal Three-Layer Film Material. *Micromachines* **2021**, *12*, 1552. https://doi.org/10.3390/mi12121552

Academic Editor: Kai Xu

Received: 13 November 2021
Accepted: 8 December 2021
Published: 12 December 2021

1. Introduction

Metamaterials are composite structures made of artificial unit structures, which can realize sensing [1,2], photocatalysis [3–5], thermal emitters [6], infrared detection and imaging equipment [7], and other applications [8,9]. Their singular properties are derived from artificially designed microstructures, rather than determined by the composition of the materials. The perfect absorption of waves can be achieved by using metamaterials. The principle is to achieve zero transmission and reflection at the frequency of interest. When the free space impedance is equal to the metamaterial impedance, the reflection is minimal. The traditional metamaterial absorber is generally composed of a metal—dielectric—metal (MDM) structure, and different absorption characteristics are obtained by designing different microstructures on the top metal [10–15]. These MDM structures have a general feature for the design of plasmon and metamaterial absorbers, with a thin dielectric interval in between, in order to realize the strong plasmon near-field coupling between the top plasmonic resonator and the bottom metal reflector. Because of the inherent high optical loss of metals, the resonant absorption bandwidths of the absorbers are relatively wide [16–23]. In addition, metals are also easy to corrode and oxidize, their structure is complex, and their preparation costs are relatively high, which limit their applications. Compared with metal materials, dielectric materials have the characteristics of a simple structure, stable performance, and low ohmic loss, which are popular in the research of metamaterials today [24]. In some applications, the difference in absorption bandwidth determines different effects. For example, broadband absorbers can effectively absorb electromagnetic energy in a wide range of wavelengths and can be used in fields such as solar absorbers [25–28]. The narrow-band absorber has a high time coherence, and this high sensitivity and figure of merit are conducive to applications in refractive index

sensors and other fields [29–32]. Recently, many researchers have conducted a series of studies on narrow-band perfect absorbers based on dielectric materials. For example, Liao et al. recently achieved perfect absorption with an absorption bandwidth of 1.3 nm through a dielectric structure set on a metal substrate [33]. Another example is that by adding a layer of Si medium to the surface of the metal grating to form a complementary structure, Wang et al. proved that adding a layer of Si complementary grating structure could effectively reduce the absorption bandwidth of the resonance peak [34]. However, the narrowest absorption bandwidth they achieved was only 5.4 nm.

This paper designs a dielectric−dielectric−metal (DDM) structure. The bottom metal plate prevents electromagnetic waves from penetrating the structure, so that the transmission is zero. The intermediate dielectric layer was a SiO_2 plane layer, and the frequency selective surface was a grating structure made of a TiO_2 dielectric material. The absorber achieves dual-band perfect absorption in the near-infrared range. The resonance peaks are located at 865.295 nm and 967.645 nm, the absorption rates are 97.6% and 99.1%, the absorption bandwidths are 11 nm and 2 nm, and the Q factors are 79 and 484, respectively. We analyzed the physical mechanism of its resonance, and also discussed the tunability of the structure and the tolerance of the working angle. By changing the environment where the absorber is located, its sensing performance could be analyzed. Our design provides a new design idea for high-Q optical devices, which can be applied to a variety of high-Q factor multispectral applications.

2. Structure Design and Numerical Model

Figure 1 shows a schematic diagram of the designed absorber. The substrate adopts a metal plane layer so that the transmission of the structure is 0, as shown in Figure 2. The dielectric property parameters are from the experimental data provided by Johnson and Christy et al. [35]. The intermediate dielectric layer is made of SiO_2 with a refractive index (RI) of 1.45. The top layer is a dielectric grating structure, using TiO_2, with a RI of 2.4 [36,37]. As material loss was not considered, the RI of the dielectric material was set to a pure real number. In the figure, the physical meaning of the structural parameters s indicated by letters. We used FDTD Solutions software for the simulation. In the simulation process, the parameters were set as: w_1 = 150 nm, w_2 = 80 nm, h_1 = 150 nm, h_2 = 350 nm, h_3 = 313 nm, and px = py = p = 600 nm. By adding time domain monitors, the transmission (T) and reflection (R) data of the structure could be obtained. According to the formula A = 1-R-T, the absorption data could be obtained [38–41]. In the simulation process, a plane light source was used for the incidence, and the x, y, and z directions were the antisymmetric, symmetric, and PML boundary conditions, respectively.

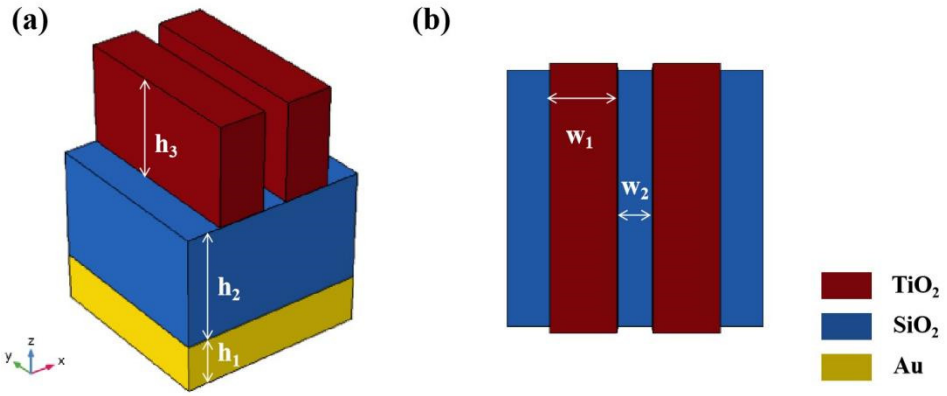

Figure 1. (**a**,**b**) Three-dimensional view and a top view of the designed absorber, respectively.

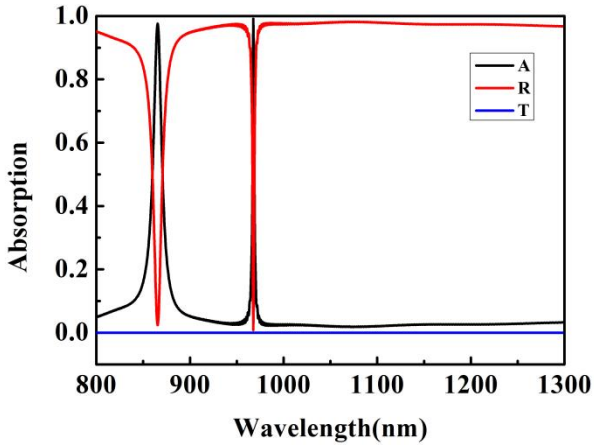

Figure 2. Spectra of R, T, and A under TM polarized light.

3. Simulations Results and Discussions

Figure 2 shows the transmission, reflection, and absorption spectra of the absorber. It can be seen that this absorber can obtain double-band perfect absorption in the near-infrared band range of 800–1300 nm. The resonance peaks are λ_1 = 865.295 nm (absorption is 97.6%) and λ_2 = 967.645 nm (absorption is 99.1%). Their full width at half maximum (FWHM) was 11 nm and 2 nm, and the Q factors were 79 and 484. It achieved ultra-sharp resonance light absorption. The absorber had the characteristics of a high Q factor, simple structure, and easy preparation. It provided a new method for the design of high-Q optical devices, and could be used in various applications, such as photon detection and spectral sensing.

Next, we calculated the electromagnetic field distribution in the two resonance modes to analyze the resonance mechanism. It can be seen from Figure 3a that the electric field at λ_1 was mainly distributed between the slits of the dielectric grating and metal surface. This shows that under the excitation of incident light, the dielectric layer excited the plasmon resonance of the metal surface. As the dielectric constants of SiO_2 and gold are very different, the vertical component of the electric field cannot penetrate deep into the metal, but only exists on the surface of the metal [42,43]. For the electric field distribution in the top layer medium, it is obvious that there are red dots with concentrated energy, which indicates that the dielectric grating structure produces magnetic polaritons (MPs), which is a typical feature of MPs resonance [44,45]. The resonance peak at λ_1 is mainly derived from the plasmon resonance of the metal. This phenomenon can be confirmed according to the magnetic field distribution in Figure 3b. Figure 3c shows the electric field distribution at λ_2. It can be clearly seen that in this resonance mode, the electric field is mainly distributed in the dielectric layer and the dielectric grating. The intensity of the plasmon resonance excited at this time is much smaller than the intensity of the medium resonance. The strong resonance peak is mainly derived from the MPs resonance supported by the dielectric material, which can be confirmed by the magnetic field distribution in Figure 3d. Comparing the electromagnetic field distribution and intensity in the two modes, it can be seen that the dielectric resonance intensity is far greater than the plasmon resonance intensity. Therefore, ultra-sharp resonance peaks can be generated in the λ_2 resonance mode. Therefore, dielectric nanoparticles also support electric resonance in metal particles and support MPs resonance. The hybrid coupling between MPs resonance and the plasmon resonance of metal can produce two sharp absorption peaks.

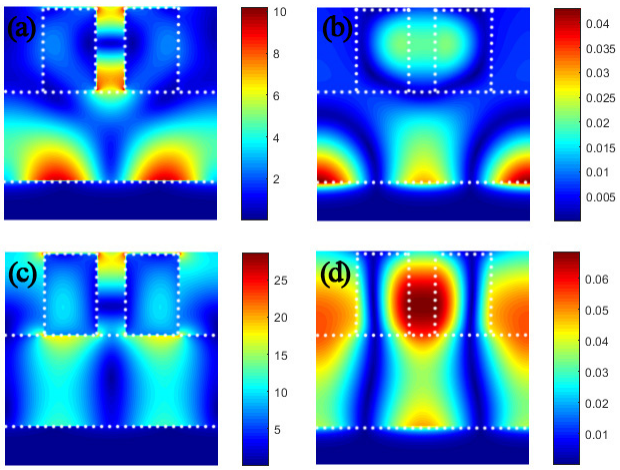

Figure 3. (**a**,**b**) Distribution of electric and magnetic fields at λ_1 = 865.295 nm. (**c**,**d**) Distribution of electric and magnetic fields at λ_2 = 967.645 nm. The white dotted lines describe the structure of the absorber.

Figure 4a–d shows the change of the absorption spectrum after transforming the geometrical parameters of the metamaterial absorber. Figure 4a shows the change of the absorption spectrum when the width of the grating stripe is changed. As the width increases, both resonance peaks show a red shift. For the resonance peak at λ_1, the absorption remains basically unchanged, while the absorption at λ_2 shows a trend of first increasing and then decreasing. Because the resonance peak in this mode is mainly caused by the MPs resonance of the dielectric grating, the width of the grating has a greater influence on the resonance peak at λ_2. Figure 4b shows the change of the absorption spectrum when the pitch of the grating stripes is changed. As the distance increases, the resonance wavelength at λ_1 produces a blue shift. The resonance wavelength at λ_2 produces a red shift, and when the distance exceeds 80 nm, the absorption begins to decrease. Therefore, there is a critical value for the grating fringe pitch. Figure 4c shows the change of the absorption spectrum when the height of the grating stripe is changed. For the resonance peak in the λ_1 mode, the resonance wavelength first shifts red and then blue as the height increases, and when h_3 = 353 nm, the absorption rate is the lowest, dropping to about 84%. For the resonant peak in λ_2 mode, the resonant peak only shows a red shift. When h_3 changes in the range of 273 nm to 313 nm, perfect absorption can still be maintained. Therefore, the height of the dielectric grating also has a critical value. When it is greater than the critical value, the absorption of the absorption peaks in both modes will be greatly reduced. Figure 4d shows the change of the absorption spectrum when the period of the absorber unit structure is changed. Only when the period is 600 nm, the two absorption peaks can achieve perfect absorption. Interestingly, when the period is 560 nm, only the resonance peak of the λ_1 mode exists. These results all show that the absorber is tunable, and different absorption functions can be achieved by changing the structural parameters. When the structural parameters are changed, the impedance of the absorber will change, and it cannot match perfectly with the impedance of free space, so it will be manifested by the reduction of absorption or the movement of the absorption peak.

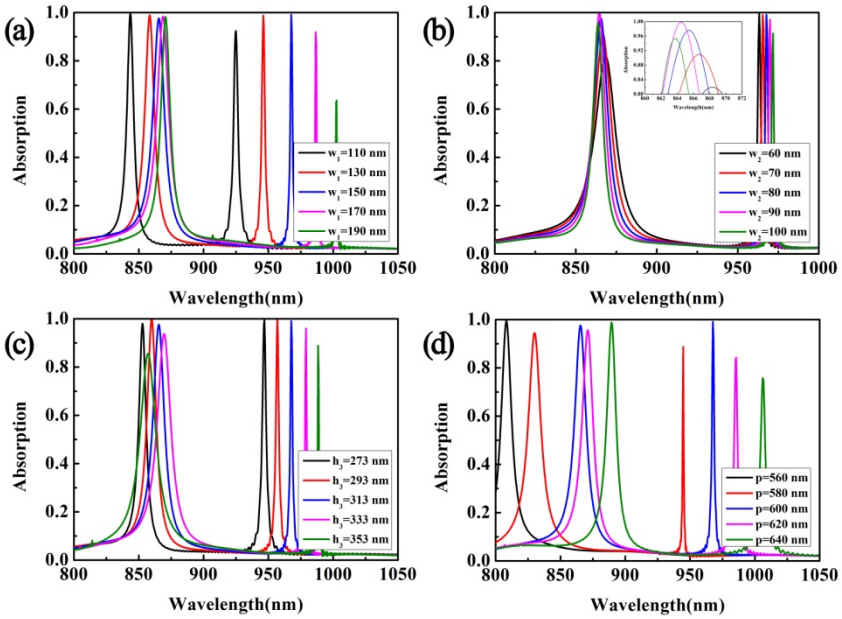

Figure 4. (**a**–**d**) The change of the absorption spectrum when changing the value of w_1, w_2, h_3, and p.

As the designed grating was a one-dimensional structure (extends infinitely along the Y direction), we only studied the working angle tolerance under TM polarized light, as shown in Figure 5. The research results show that the structure could only maintain good absorption characteristics in the range of a 0–15° incident angle, and its absorption peaks position, absorption intensity, and absorption bandwidth remain unchanged. This indicates that within this range, the structure was insensitive to the incident angle.

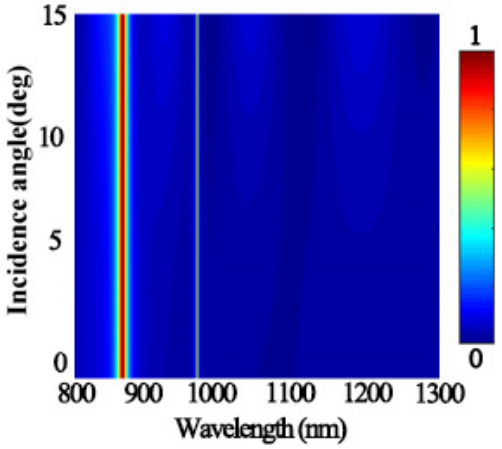

Figure 5. Corresponding resonance wavelengths at different incident angles.

Finally, in order to analyze the sensing performance of the designed dual-band perfect metamaterial absorber, with the other parameters unchanged, we calculated the absorption spectrum under different environmental RIs. The results are shown in Figure 6a. When the RI increases, the resonance peaks at λ_1 and λ_2 both show a red shift, the absorption at λ_1 increases slightly, while the absorption at λ_2 shows a downward trend. For the resonance peak at λ_1, the resonance wavelength changes from 865.295 nm to 867.825 nm, and the change is only 2.53 nm. For the resonance peak at λ_2, the resonance wavelength changes from 967.645 nm to 975.824 nm, and the amount of change is 8.179 nm. The resonance wavelengths of the absorber under different RIs were extracted and numerically fitted. Figure 6b,c shows the results. It can be clearly seen from the figure that for the

two resonance modes, there is a linear relationship between their resonance wavelength and RI. Analyzing the sensitivity ($S = \Delta\lambda/\Delta n$) and figure of merit (FOM = S/FWHM) of the two modes can get S_1 = 50 nm/RIU and S_2 = 165 nm/RIU, and FOM_1 = 5 1/RIU and FOM_2 = 83 1/RIU [46–50], respectively. It can be seen that the absorber has a good sensing performance and can be used in refractive index sensors and other fields. Comparing the performance parameters of our proposed absorber with the previous work, as shown in Table 1, it clearly shows the advantage of a high Q factor [51–54]. Therefore, it is also suitable for various high-Q factor multi-spectral applications, such as photon detection, spectral sensing, and other fields.

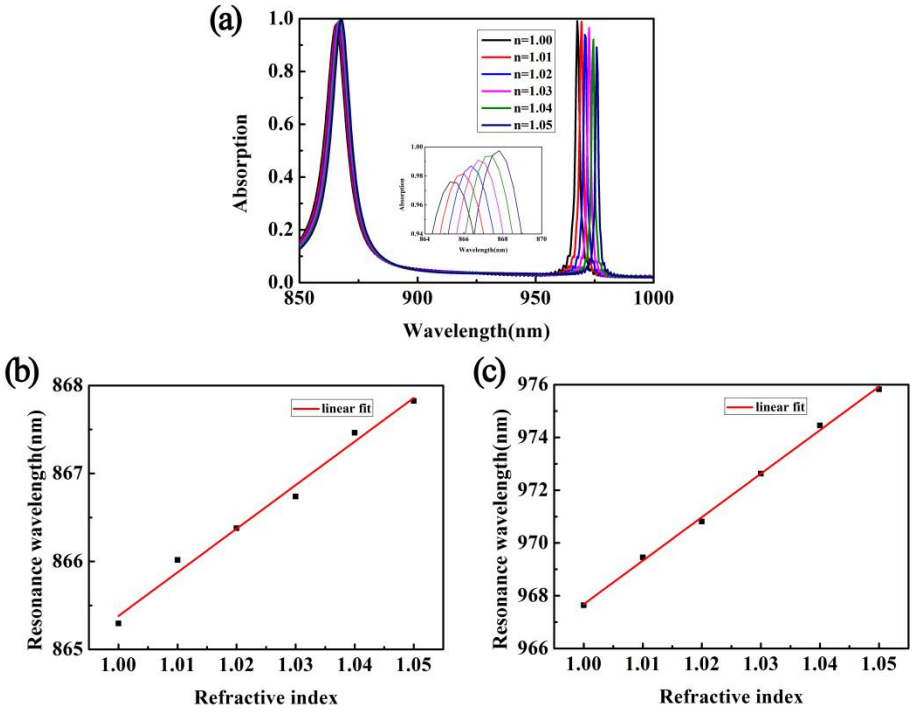

Figure 6. (**a**) The numerical calculation results of the absorption spectrum when the RI of the environment changes. (**b**,**c**) Linear relationships between the resonance wavelength and the RI in the λ_1 and λ_2 modes, respectively.

Table 1. Comparison of the maximum FOM and Q value of the absorber reported in this paper with the results of the dual-band absorber reported by other works.

Reference	[51]	[52]	[53]	[54]	Proposed
FOM (max) (1/RIU)	16.54	26.67	44.5	12.16	83
Q (max)	19.8	23.33	123.45	71.42	484

4. Conclusions

In general, this article achieved dual-band narrowband absorption by designing a dielectric structure on a metal substrate, and obtained a high Q factor of 484. The ultra-sharp light absorption comes from the hybrid coupling between MPs resonance and plasmon resonance. The research results show that the absorber is tunable. When the size and height of the top dielectric grating and the unit structure period are changed, the position and intensity of the resonance peak will change. The maximum working angle tolerance can reach 15°. The sensitivity and FOM of the two resonance modes are S_1 = 50 nm/RIU and S_2 = 165 nm/RIU, and FOM_1 = 5 1/RIU and FOM_2 = 83 1/RIU, respectively. It has a good sensing performance. It can be applied to high Q factor multi-spectral applications, such as photon detection, sensor filtering, and other fields.

Author Contributions: B.L.: conceptualization, formal analysis, investigation, data curation, and writing—original draft, review, and editing. P.W., conceptualization, formal analysis, investigation, data curation, and funding acquisition. H.Z., conceptualization, formal analysis, and revision. L.L. conceptualization, formal analysis, and revision. All authors have read and agreed to the published version of the manuscript.

Funding: This research received no external funding.

Acknowledgments: This work is supported by the National Natural Science Foundation of China (11774128 and 11704223), and the Natural Science Foundation of Shandong Province (ZR2018JL003 and 2019KJJ003).

Conflicts of Interest: The authors declare no conflict of interest.

References

1. Li, Z.; Yi, Z.; Liu, T.; Liu, L.; Chen, X.; Zheng, F.; Zhang, J.; Li, H.; Wu, P.; Yan, P. Three-band perfect absorber with high refractive index sensing based on an active tunable Dirac semimetal. *Phys. Chem. Chem. Phys.* **2021**, *23*, 17374–17381. [CrossRef] [PubMed]
2. Wu, X.L.; Zheng, Y.; Luo, Y.; Zhang, J.G.; Yi, Z.; Wu, X.W.; Cheng, S.; Yang, W.; Yue, Y.; Wu, P. A four-band and polarization-independent BDS-based tunable absorber with high refractive index sensitivity. *Phys. Chem. Chem. Phys.* **2021**, *23*, 26864–26873. [CrossRef]
3. Xiao, L.; Zhang, Q.; Chen, P.; Chen, L.; Ding, F.; Tang, J.; Li, Y.-J.; Au, C.-T.; Yin, S.-F. Copper-mediated metal-organic framework as efficient photocatalyst for the partial oxidation of aromatic alcohols under visible-light irradiation: Synergism of plasmonic effect and schottky junction. *Appl. Catal. B Environ.* **2019**, *248*, 380–387. [CrossRef]
4. Chen, P.; Liu, F.; Ding, H.; Chen, S.; Chen, L.; Li, Y.-J.; Au, C.-T.; Yin, S.-F. Porous double-shell CdS@C3N4 octahedron derived by in situ supramolecular self-assembly for enhanced photocatalytic activity. *Appl. Catal. B Environ.* **2019**, *252*, 33–40. [CrossRef]
5. Cheng, T.T.; Gao, H.J.; Liu, G.R.; Pu, Z.S.; Wang, S.F.; Yi, Z.; Wud, X.; Yanga, H. Preparation of core-shell heterojunction photocatalysts by coating CdS nanoparticles onto $Bi_4Ti_3O_{12}$ hierarchical microspheres and their photocatalytic removal of organic pollutants and Cr(VI) ions. *Colloids Surf. A Physicochem. Eng. Asp.* **2021**, *633*, 127918. [CrossRef]
6. Zhou, F.; Qin, F.; Yi, Z.; Yao, W.-T.; Liu, Z.; Wu, X.; Wu, P. Ultra-wideband and wide-angle perfect solar energy absorber based on Ti nanorings surface plasmon resonance. *Phys. Chem. Chem. Phys.* **2021**, *23*, 17041–17048. [CrossRef]
7. Xiao, D.; Tao, K. Ultra-compact metamaterial absorber for multiband light absorption at mid-infrared frequencies. *Appl. Phys. Express* **2015**, *8*, 102001. [CrossRef]
8. Sayem, A.A.; Mahdy, M.R.C.; Jahangir, I.; Rahman, M.S. Ultrathin ultra-broadband electro-absorption modulator based on few-layer graphene based anisotropic metamaterial. *Opt. Commun.* **2017**, *384*, 50–58. [CrossRef]
9. Ogawa, S.; Okada, K.; Fukushima, N.; Kimata, M. Wavelength selective uncooled infrared sensor by plasmonics. *Appl. Phys. Lett.* **2012**, *100*, 021111. [CrossRef]
10. Ogawa, S.; Masuda, K.; Takagawa, Y.; Kimata, M. Polarization-selective uncooled infrared sensor with asymmetric two-dimensional plasmonic absorber. *Opt. Eng.* **2014**, *53*, 107110. [CrossRef]
11. Li, R.; Zheng, Y.; Luo, Y.; Zhang, J.; Yi, Z.; Liu, L.; Song, Q.; Wu, P.; Yu, Y.; Zhang, J. Multi-peak narrow-band perfect absorber based on two-dimensional graphene array. *Diam. Relat. Mater.* **2021**, *120*, 108666. [CrossRef]
12. Jiang, L.; Yi, Y.; Tang, Y.; Li, Z.; Yi, Z.; Liu, L.; Chen, X.; Jian, R.; Wu, P.; Yan, P. A high quality factor ultra-narrow band perfect metamaterial absorber for monolayer molybdenum disulfide. *Chin. Phys. B* **2021**, *19*, 103415. [CrossRef]
13. Li, J.; Jiang, J.; Zhao, D.; Xu, Z.; Liu, M.; Liu, X.; Tong, H.; Qian, D. Novel hierarchical sea urchin-like Prussian blue@palladium core–shell heterostructures supported on nitrogen-doped reduced graphene oxide: Facile synthesis and excellent guanine sensing performance. *Electrochim. Acta* **2020**, *330*, 135196. [CrossRef]
14. Lin, X.; Li, Y.J.; Chen, F.T.; Xu, P.; Li, M. Facile synthesis of mesoporous titanium dioxide doped by Ag-coated graphene with enhanced visible-light photocatalytic performance for methylene blue degradation. *RSC Adv.* **2017**, *7*, 25314–25324. [CrossRef]
15. Xu, F.; Lin, L.; Wei, D.; Xu, J.; Fang, J. An Asymmetric Silicon Grating Dual-Narrow-Band Perfect Absorber Based on Dielectric-Metal-Dielectric Structure. *Front. Mater.* **2021**, *8*, 752745. [CrossRef]
16. Huang, M.; Wei, K.; Wu, P.; Xu, D.; Xu, Y. Design of Grating Type GaAs Solar Absorber and Investigation of Its Photoelectric Characteristics. *Front. Mater.* **2021**, *8*, 781803. [CrossRef]
17. Jiang, L.Y.; Yi, Y.T.; Yi, Z.; Yang, H.; Li, Z.Y.; Su, J.; Zhou, Z.G.; Chen, X.F.; Yi, Y.G. A four-band perfect absorber based on high quality factor and high figure of merit of monolayer molybdenum disulfide. *Acta Phys. Sin.* **2021**, *70*, 128101. [CrossRef]
18. Li, J.; Chen, X.; Yi, Z.; Yang, H.; Tang, Y.; Yi, Y.; Yao, W.; Wang, J.; Yi, Y. Broadband solar energy absorber based on monolayer molybdenum disulfide using tungsten elliptical arrays. *Mater. Today Energy* **2020**, *16*, 100390. [CrossRef]
19. Li, Y.; Li, M.; Xu, P.; Tang, S.; Liu, C. Efficient photocatalytic degradation of acid orange 7 over N-doped ordered mesoporous titania on carbon fibers under visible-light irradiation based on three synergistic effects. *Appl. Catal. A Gen.* **2016**, *524*, 163–172. [CrossRef]

20. Li, J.; Jiang, J.; Xu, Z.; Liu, M.; Tang, S.; Yang, C.; Qian, D. Facile synthesis of Ag@Cu_2O heterogeneous nanocrystals decorated N-doped reduced graphene oxide with enhanced electrocatalytic activity for ultrasensitive detection of H_2O_2. *Sens. Actuators B Chem.* **2018**, *260*, 529–540. [CrossRef]
21. Cheng, Z.; Liao, J.; He, B.; Zhang, F.; Zhang, F.; Huang, X.; Zhou, L. One-Step Fabrication of Graphene Oxide Enhanced Magnetic Composite Gel for Highly Efficient Dye Adsorption and Catalysis. *ACS Sustain. Chem. Eng.* **2015**, *3*, 1677–1685. [CrossRef]
22. Yi, Z.; Li, J.; Lin, J.; Qin, F.; Chen, X.; Yao, W.; Liu, Z.; Cheng, S.; Wu, P.; Li, H. Broadband polarization-insensitive and wide-angle solar energy absorber based on tungsten ring-disc array. *Nanoscale* **2020**, *12*, 23077–23083. [CrossRef] [PubMed]
23. Su, J.; Yang, H.; Xu, Y.; Tang, Y.; Yi, Z.; Zheng, F.; Zhao, F.; Liu, L.; Wu, P.; Li, H. Based on Ultrathin PEDOT: PSS/c-Ge Solar Cells Design and Their Photoelectric Performance. *Coatings* **2021**, *11*, 748. [CrossRef]
24. Jiang, L.; Yuan, C.; Li, Z.; Su, J.; Yi, Z.; Yao, W.; Wu, P.; Liu, Z.; Cheng, S.; Pan, M. Multi-band and high-sensitivity perfect absorber based on monolayer graphene metamaterial. *Diam. Relat. Mater.* **2021**, *111*, 108227. [CrossRef]
25. Yu, P.; Yang, H.; Chen, X.; Yi, Z.; Yao, W.; Chen, J.; Yi, Y.; Wu, P. Ultra-wideband solar absorber based on refractory titanium metal. *Renew. Energy* **2020**, *158*, 227–235. [CrossRef]
26. Cui, Y.; Fung, K.H.; Xu, J.; Ma, H.; Jin, Y.; He, S.; Fang, N.X. Ultrabroadband Light Absorption by a Sawtooth Anisotropic Metamaterial Slab. *Nano Lett.* **2012**, *12*, 1443–1447. [CrossRef]
27. Liu, Y.; Bo, M.; Yang, X.; Zhang, P.; Sun, C.Q.; Huang, Y. Size modulation electronic and optical properties of phosphorene nanoribbons: DFT–BOLS approximation. *Phys. Chem. Chem. Phys.* **2017**, *19*, 5304–5309. [CrossRef]
28. Qin, F.; Chen, X.F.; Yi, Z.; Yao, W.T.; Yang, H.; Tang, Y.J.; Yi, Y.; Li, H.; Yi, Y. Ultra-broadband and wide-angle perfect solar absorber based on TiN nanodisk and Ti thin film structure. *Sol. Energy Mater. Sol. Cells* **2020**, *211*, 110535. [CrossRef]
29. Li, Z.Y.; Butun, S.; Aydin, K. Ultranarrow Band Absorbers Based on Surface Lattice Resonances in Nanostructured Metal Surfaces. *ACS Nano* **2014**, *8*, 8242–8248. [CrossRef]
30. Long, F.; Zhang, Z.; Wang, J.; Yan, L.; Zhou, B. Cobalt-nickel bimetallic nanoparticles decorated graphene sensitized imprinted electrochemical sensor for determination of octylphenol. *Electrochim. Acta* **2015**, *168*, 337–345. [CrossRef]
31. Cai, L.; Zhang, Z.; Xiao, H.; Chen, S.; Fu, J. An eco-friendly imprinted polymer based on graphene quantum dots for fluorescent detection of p-nitroaniline. *RSC Adv.* **2019**, *9*, 41383–41391. [CrossRef]
32. Chen, Z.; Chen, H.; Yin, J.; Zhang, R.; Jile, H.; Xu, D.; Yi, Z.; Zhou, Z.; Cai, S.; Yan, P. Multi-band, tunable, high figure of merit, high sensitivity single-layer patterned graphene—Perfect absorber based on surface plasmon resonance. *Diam. Relat. Mater.* **2021**, *116*, 108393. [CrossRef]
33. Liao, Y.L.; Zhao, Y.; Zhang, X.F.; Chen, Z.G. An ultra-narrowband absorber with a compound dielectric grating and metal substrate. *Opt. Commun.* **2017**, *385*, 172–176. [CrossRef]
34. Wang, X.; Zhu, J.; Xu, Y.; Qi, Y.; Zhang, L.; Yang, H.; Yi, Z. A novel plasmonic refractive index sensors based on schottky junction with gold/silicon complementary grating structure. *Chin. Phys. B* **2021**, *30*, 024207. [CrossRef]
35. Johnson, P.B.; Christy, R.W. Optical constants of the noble metals. *Phys. Rev. B* **1972**, *6*, 4370–4379. [CrossRef]
36. Nie, J.; Yu, J.; Liu, W.; Yu, T.; Gao, P. Ultra-narrowband perfect absorption of monolayer two-dimensional materials enabled by all-dielectric subwavelength gratings. *Opt. Express* **2020**, *28*, 38592. [CrossRef]
37. Deng, Y.; Cao, G.; Wu, Y.; Zhou, X.; Liao, W. Theoretical Description of Dynamic Transmission Characteristics in MDM Waveguide Aperture-Side-Coupled with Ring Cavity. *Plasmonics* **2015**, *10*, 1537–1543. [CrossRef]
38. Cao, G.; Li, H.; Deng, Y.; Zhan, S.; He, Z.; Li, B. Systematic Theoretical Analysis of Selective-Mode Plasmonic Filter Based on Aperture-Side-Coupled Slot Cavity. *Plasmonics* **2014**, *9*, 1163–1169. [CrossRef]
39. Lv, P.; Xie, D.; Zhang, Z. Magnetic carbon dots based molecularly imprinted polymers for fluorescent detection of bovine hemoglobin. *Talanta* **2018**, *188*, 145–151. [CrossRef]
40. Zhang, Z.; Cai, R.; Long, F.; Wang, J. Development and application of tetrabromobisphenol A imprinted electrochemical sensor based on graphene/carbon nanotubes three-dimensional nanocomposites modified carbon electrode. *Talanta* **2015**, *134*, 435–442. [CrossRef]
41. Cai, R.; Rao, W.; Zhang, Z.; Long, F.; Yin, Y. An imprinted electrochemical sensor for bisphenol A determination based on electrodeposition of a graphene and Ag nanoparticle modified carbon electrode. *Anal. Methods* **2014**, *6*, 1590–1597. [CrossRef]
42. Deng, Y.; Cao, G.; Yang, H.; Zhou, X.; Wu, Y. Dynamic Control of Double Plasmon-Induced Transparencies in Aperture-Coupled Waveguide-Cavity System. *Plasmonics* **2018**, *13*, 345–352. [CrossRef]
43. Chen, H.-J.; Zhang, Z.-H.; Cai, R.; Kong, X.-Q.; Chen, X.; Liu, Y.-N.; Yao, S.-Z. Molecularly imprinted electrochemical sensor based on a reduced graphene modified carbon electrode for tetrabromobisphenol A detection. *Analyst* **2013**, *138*, 2769–2776. [CrossRef] [PubMed]
44. Tang, N.; Li, Y.; Chen, F.; Han, Z. In situ fabrication of a direct Z-scheme photocatalyst by immobilizing CdS quantum dots in the channels of graphene-hybridized and supported mesoporous titanium nanocrystals for high photocatalytic performance under visible light. *RSC Adv.* **2018**, *8*, 42233–42245. [CrossRef]
45. Li, Z.; Yi, Y.; Xu, D.; Yang, H.; Yi, Z.; Chen, X.; Yi, Y.; Zhang, J.; Wu, P. A multi-band and polarization-independent perfect absorber based on Dirac semimetals circles and semi-ellipses array. *Chin. Phys. B* **2021**, *30*, 098102. [CrossRef]
46. Yang, X.; Zhang, F.; Hu, Y.J.; Chen, D.Z.; He, Z.Q.; Xiong, L.Z. Gold nanoparticals doping graphene sheets nanocomposites sensitized screen-printed carbon electrode as a disposable platform for voltammetric determination of guaiacol in bamboo juice. *Int. J. Electrochem. Sci.* **2014**, *9*, 5061–5072.

47. Liu, H.; Wang, Q.; Zhang, F. Preparation of Fe_3O_4@SiO_2@P(AANa-co-AM) composites and their adsorption for Pb (II). *ACS Omega* **2020**, *5*, 8816–8824. [CrossRef]
48. Chen, S.; Zhou, S.; Fu, J.L.; Tang, S.S.; Wu, X.D.; Zhao, P.F.; Zhang, Z.H. A near infrared fluorescence imprinted sensor based on zinc oxide nanorods for rapid determination of ketoprofen. *Anal. Methods* **2021**, *13*, 2836–2846. [CrossRef] [PubMed]
49. Chen, S.; Fu, J.L.; Zhou, S.; Wu, X.D.; Tang, S.S.; Zhao, P.F.; Zhang, Z.H. An eco-friendly near infrared fluorescence molecularly imprinted sensor based on zeolite imidazolate framework-8 for rapid determination of trace trypsin. *Microchem. J.* **2021**, *168*, 106449. [CrossRef]
50. Chen, Z.; Chen, H.; Jile, H.; Xu, D.; Yi, Z.; Lei, Y.; Chen, X.; Zhou, Z.; Cai, S.; Li, G. Multi-band multi-tunable perfect plasmon absorber based on L-shaped and double-elliptical graphene stacks. *Diam. Relat. Mater.* **2021**, *115*, 108374. [CrossRef]
51. Cheng, Y.; Zhang, Y.H.; Mao, X.S.; Guo, R. Dual-band plasmonic perfect absorber based on all-metal nanostructure for refractive index sensing application. *Mater. Lett.* **2018**, *219*, 123–126. [CrossRef]
52. Chou Chau, Y.F.; Chou Chao, C.T.; Huang, H.J.; Kooh, M.R.; Kumara, N.T.R.N.; Lim, C.M.; Chiang, H.P. Perfect Dual-Band Absorber Based on Plasmonic Effect with the Cross-Hair/Nanorod Combination. *Nanomaterials* **2020**, *10*, 493. [CrossRef]
53. Alipour, A.; Mir, A.; Farmani, A. Ultra high-sensitivity and tunable dual-band perfect absorber as a plasmonic sensor. *Optics Laser Technol.* **2020**, *127*, 106201. [CrossRef]
54. Liu, Y.; Zhang, Y.Q.; Jin, X.R.; Zhang, S.; Lee, Y.P. Dual-band infrared perfect absorber for plasmonic sensor based on the electromagnetically induced reflection-like effect. *Opt. Commun.* **2016**, *371*, 173–177. [CrossRef]